Discover Oncology

RESEARCH Open Access

PXMP2 inhibits tumor stemness and immune infiltration in hepatocellular carcinoma based on stemness risk

Dingde Ye[1,2†], Jiaqing Chen[1,2†], Jian Wang[1], Qing Ge[1], Xianzhong He[1], Jiamu Qu[4], Ting Fang[1], Runze Wang[1], Shuai Mao[1,2,3], Qiang Wang[1,2,3*], Qingxiang Xu[1,2,3*] and Beicheng Sun[1,2,3*]

†Dingde Ye and Jiaqing Chen are equally contribute this work.

*Correspondence:
Qiang Wang
wangqiang@ahmu.edu.cn
Qingxiang Xu
xqx@ahmu.edu.cn
Beicheng Sun
sunbc@ahmu.edu.cn
[1]Department of Hepatobiliary Surgery, The First Affiliated Hospital of Anhui Medical University, Hefei, Anhui, China
[2]MOE Innovation Center for Basic Research in Tumor Immunotherapy, Hefei, Anhui, China
[3]Anhui province key laboratory of tumor immune Microenvironment and immunotherapy, Hefei, Anhui, China
[4]Southeast University, Nanjing 210009, China

Abstract

Background Hepatocellular carcinoma (HCC) is a complex and heterogeneous disease wherein cancer stem cells (CSCs) play a pivotal role in driving tumorigenesis, metastasis, and resistance to therapy. This study sought to map the stemness landscape of HCC and identify patients who may benefit from immunotherapy.

Methods A total of 26 stem cell gene sets were obtained from the StemChecker database. A stemness risk model was constructed based on data from TCGA, GEO databases, and bioinformatics methods. The hub genes identified in the model underwent significant preliminary in *vitro* and in *vivo* phenotypic validation, which included evaluating their effects on tumor stemness and their functional roles and interactions in TME. This basic verification emphasized the clinical relevance of hub genes and confirmed the practicality of the model in HCC stemness risk assessment and immune infiltration risk assessment, thereby providing a basis for potential treatment strategies.

Results HCC patients exhibited three subtypes; C1 showed the worst prognosis, which was linked to high stemness risk and immunosuppressive features. The hub gene *PXMP2* demonstrated tumor-suppressive properties by inhibiting tumor stemness in both in vitro and in vivo experiments, promoting the infiltration of anti-tumor M1 macrophages while simultaneously suppressing the infiltration of immunosuppressive M2 macrophages and neutrophils. Moreover, the high expression of PXMP2 was correlated with a favorable prognosis for the patients.

Conclusions This study identified three distinct stemness-based subtypes of HCC and established a novel three-gene prognostic risk model. Our findings highlight the critical role of PXMP2 in tumor biology and its potential as a therapeutic target, paving the way for personalized immunotherapy and chemotherapy approaches to enhance clinical outcomes in HCC patients.

Keywords Hepatocellular carcinoma, Cancer stem cells, Bioinformatics, Tumor microenvironment, Immunotherapy

1 Introduction

Hepatocellular carcinoma (HCC) is one of the most prevalent liver cancers, marked by a high incidence and a poor prognosis [1]. Surgical resection is considered an effective treatment for early stage HCC [2]. However, despite the availability of diverse treatment modalities, such as surgical resection, liver transplantation, ablation, and chemotherapy, their effectiveness is often hindered by the high recurrence rates and limited accessibility to surgery or transplantation due to the typically late-stage diagnosis of the disease [3–5].

Cancer stem cells (CSCs) exhibit characteristics akin to normal stem cells, including self-renewal and differentiation potential [6]. Different types of CSCs have been identified in various malignancies, such as lung cancer, pancreatic cancer, breast cancer, prostate cancer, colon cancer, gliomas, and HCCs [7–10]. CSCs are highly tumorigenic, metastatic, and resistant to both chemotherapy and radiation, which contributes significantly to tumor relapse after treatment. Moreover, CSCs can evade multidrug resistance through diverse intrinsic and extrinsic pathways [11].

The CSCs specific to HCC are known as liver CSCs (LCSCs). LCSCs display tissue-specific traits, including tumorigenesis, chemoresistance, metastasis, and recurrence, often mirroring the phenotypes observed in xenotransplanted tumors [12]. These cells are instrumental in drug tolerance, facilitating both metastasis and recurrence [13]. When compared to other tumor cell types, LCSCs exhibited superior internal circulation capabilities, which enhance their ability to metastasize and establish secondary tumors. This unique ability contributes to HCC recurrence by promoting the growth of primary cancer cells and facilitating the spread of secondary malignancies [14]. Consequently, LCSCs are strongly associated with metastasis, recurrence, and multidrug resistance, making them valuable diagnostic markers for HCC. Recent research has increasingly focused on targeting LCSCs to mitigate tumor recurrence [15].

In this study, we analyzed HCC patient transcriptomes for stemness using ssGSEA on 26 gene sets, classifying patients into three subtypes with distinct survival outcomes and tumor microenvironment (TME) patterns. A Stemness Subtype predictor was developed and validated in independent cohorts. WGCNA identified hub genes linked to stemness and prognosis, which were further validated through in vitro experiments, including cell proliferation, migration assays, and stemness-related marker expression analysis. Additionally, in vivo experiments utilized HCC xenograft models to assess tumor growth and metastasis, confirming the functional relevance of identified genes in the stemness subtypes.

In conclusion, our study findings facilitate individualized survival predictions and provide better treatment options for physicians and HCC patients based on the novel stemness-based model and molecular classification.

2 Materials and methods

2.1 Clinical samples and data acquisition

The RNA expression profiles were obtained from the GEO database (https://www.ncbi.nlm.nih.gov/geo/) (GSE116174/GSE76427) and the TCGA database ($n = 342$) (https://cancergenome.nih.gov/). The inclusion criteria of LIHC samples were as follows: (i) gene expression profiling of LIHC were available in the dataset; (ii) complete clinical data of LIHC patients were required, including gender, age, TNM stage, and overall survival.

Finally, a total of 342 LIHC patients were enrolled in the study. Two independent datasets from the GEO database were used in this study, including GSE116174 and GSE76427 datasets. The GSE116174 included 64 HCC samples, and GSE76427 included 115 HCC samples with available clinical information. For validation purposes, data from the ICGC database (https://icgc.org/) were also used. COMBAT algorithm (empirical Bayes frame work) was applied to harmonize distributions between TCGA/GEO/ICGC datasets. The single-cell RNA sequencing (scRNA-seq) data were obtained from the GEO database (accession number: GSE149614).

2.2 Stemness signatures, TME exploration, and prognostic modeling in HCC

This study gathered 26 stem gene sets(e.g., *Hs_EC_Skotheim*, *Hs_ESC_Sato*) and employed ssGSEA for enrichment scoring, followed by consensus clustering of HCC samples. The TME characteristics were analyzed using ESTIMATE and IOBR tools. Chemotherapy sensitivity was predicted via TIDE and IC50 calculations. A prognostic stemness model was constructed based on Cox regression analysis, validated by time-dependent ROC curves, and evaluated using clinical decision curve analysis (DCA). The mRNA expression-based stemness index (mRNAsi) was derived via one-class logistic regression (OCLR). Furthermore, weighted gene co-expression network analysis (WGCNA) identified clinically relevant hub genes, with co-expression modules (e.g., palevioletred3) generated by clustering genes sharing similar expression patterns.

2.3 Cell culture

Hep3B and 293T cells were purchased from the Cell Bank of the Chinese Science Academy. Hep3B and 293T cells were cultured in Dulbecco's modified Eagle's medium (DMEM; WISENT, 319-005-CL) containing 10% fetal bovine serum (FBS; WISENT, 086–150) and 1% penicillin and streptomycin (WISENT, 450-201-EL) at 37 °C with 5% CO_2.

2.4 Plasmid construction and lentiviral packaging

shRNA sequences targeting the gene of interest were retrieved from an experimentally verified online database. Restriction enzyme sites were added, and double-stranded DNA oligos were synthesized to create shRNA expression constructs with sticky ends. The pSicoR-mCherry vector was linearized using HpaI and XhoI to produce asymmetric sticky ends, into which the shRNA constructs were inserted and transformed into competent *Escherichia coli* cells. Positive clones were confirmed by PCR and sequencing, yielding a plasmid containing the shRNA scaffold.

For lentivirus packaging, the Lenti-X™ HTX system (Clontech) was used. Lenti-X 293T cells were seeded at $4–5 \times 10^6$ cells per 100-mm plate and incubated overnight. Following the manufacturer's protocol, the transfection reagent and polymer were mixed, added to the cells, and incubated. After 4 h of incubation, the medium was changed, and the cells were cultured for an additional 48 h. The viral supernatant was harvested, centrifuged at 500 *xg* for 10 min to eliminate debris, and stored at -80 °C. Viral titer was assessed using Lenti-X GoStix™ or a serial dilution method, and the infection efficiency was calculated to determine the titer.

2.5 Quantitative reverse transcription PCR

The total RNA of the cells was extracted by using the Total RNA Isolation Kit (Vazyme, RC101- 01) and reverse transcribed into cDNA by using the Reverse Transcription Kit (Vazyme, R223). Quantitative PCR was performed with SYBR Green (Q221; Vazyme) on the QuantStudio 6 Flex Real-Time PCR System (Applied Biosystems, CA, USA). All experiments were independently repeated at least three times. GAPDH were used as an endogenous control to normalize the relative expressions. The primers used in the study are listed in the Supplementary Table S3.

2.6 Western blotting

The cells were washed thrice with PBS and lysed in RIPA buffer (Beyotime, P0013B) containing phosphatase and protease inhibitors. The cell extracts were electrophoresed using sodium dodecyl sulfate-polyacrylamide gel electrophoresis (SDS-PAGE) and subsequently transferred onto polyvinylidene fluoride membranes. The membranes were then blocked with milk for 1 h and then incubated with the corresponding primary antibodies overnight at 4 °C. The membranes were washed thrice with TBST and incubated with the corresponding secondary antibodies at room temperature. Protein bands were detected by using the ChemiDocTM MP Imaging System (Bio-Rad). All experiments were independently repeated at least three times. The antibodies used in this study are listed in Supplementary Table S4.

2.7 Multiplex immunohistochemistry staining

Clinical samples were obtained with informed consent from 90 HCC patients who underwent surgery between 2016 and 2018 at the First Affiliated Hospital of Anhui Medical University (AHMU). Tissue microarrays were constructed from paraffin-embedded cancerous and adjacent non-tumor tissues. In the study, all experimental procedures were approved by the Ethics Committee of The First Affiliated Hospital of Anhui Medical University and conformed to the requirements of the Declaration of Helsinki and the International Ethical Guidelines for Biomedical Research Involving Human Subjects(Approval No.: LLSC20221301). The tissue samples were stained using the PANO 7-plex multicolor immunofluorescence kit (Panovue, 0004100100) according to the manufacturer's instructions. The sections were incubated with the primary antibodies. These samples were then incubated with the corresponding secondary antibodies. The nuclei were stained with DAPI (Vector, H-1200-10), and photos were taken using a fluorescence scanning microscope (Olympus, BX-UCB).

2.8 Tumor cell spheroid formation assay

Liver cancer cells in the logarithmic growth phase were digested with trypsin. After detachment, the cells were centrifuged to remove trypsin and washed thrice with sterile PBS. The cells were then resuspended in DMEM/F12 (ThermoFisher, 11320033) to prepare a single-cell suspension, supplemented with 4 μg/mL heparin, 4 μg/mL heparin B27, 20 ng/mL recombinant human EGF, and 20 ng/mL recombinant human FGF. Cells were seeded in low-attachment 96-well plates at densities of 500, 400, 300, 200, and 100 cells/mL, with at least three replicate wells per concentration. The cells were cultured for 10 to 14 days. Spheroid formation was observed under a microscope, and the images were captured to assess and count the spheroids from day 0 to day 14.

2.9 Cell colony formation assay

Liver cancer cells in the logarithmic growth phase were digested with trypsin, centrifuged, and resuspended in sterile PBS to create a single-cell suspension, which was mixed with DMEM containing 10% fetal bovine serum. Approximately 200 cells were plated in each well of a 6-well plate (with at least three replicate wells per sample) and incubated at 37 °C in a 5% CO_2 atmosphere with saturated humidity for 2–3 weeks until visible colonies appeared. The supernatant was discarded, and the wells were washed twice with sterile PBS.

Next, 2 mL of paraformaldehyde was added for fixation for at least 30 min, followed by the removal of the fixative and the addition of the crystal violet staining solution for 10–30 min. Excess dye was washed off with running water, and the plates were air-dried. A transparent grid overlay was placed on top for direct colony counting, or colonies with >50 cells were enumerated under a low-power microscope. The colony formation rate was calculated using the following formula:

$$\text{Colony Formation Rate} = (\text{Number of Colonies}/\text{Number of Inoculated Cells}) \times 100\%$$

2.10 Extreme limiting dilution assay

shPXMP2-stable 3B cell lines and control 3B cell lines were seeded at densities of 25, 50, 100, 250, 500, and 1000 cells/well in uncoated 96-well ultra-low attachment plates (Corning Inc., Corning; NY, USA). The serum-free stem cell medium was refreshed weekly. The spheres were allowed to grow for 14 days before manual scoring of the 60 inner wells. Extreme limiting dilution analysis was conducted using publicly available software from the Extreme Limiting Dilution Analysis website [16].

2.11 Cell migration and invasion assay

For the migration assay, no Matrigel (Corning® Matrigel, #356234) was used. In the invasion assay, frozen Matrigel was thawed at 4 °C for 24 h, diluted 1:40 in serum-free medium, and 100 µL of the mixture was spread on the upper chamber surface, with at least three replicate wells per concentration, followed by incubation at 37 °C for 1–2 h to solidify.

Liver cancer cells were digested with trypsin, washed thrice with serum-free medium, and counted. The cells were resuspended at a density of 1×10^6 cells/mL. In a 24-well plate, 500 µL of DMEM with 10% fetal bovine serum was added, and the Matrigel-coated upper chamber was washed with the serum-free medium before adding 100 µL of the cell suspension. The cells were incubated at 37 °C in a 5% CO_2 atmosphere for 24 h.

After incubation, the transwell chambers were removed, the medium was discarded, and the chambers were washed twice with sterile PBS. They were then fixed with 500 µL of 4% paraformaldehyde for 30 min. After removing the fixative, the cells were stained with 0.1–0.2% crystal violet for 5–10 min at room temperature, washed thrice with PBS, and the upper surface cells were wiped off with cotton swabs. Six random fields were observed under a microscope at high magnification for cell counting and statistical analysis.

2.12 Blood vessel ring formation assay

The cells from both experimental and control groups were cultured in the logarithmic growth phase and harvested at equal numbers (100,000 to 200,000). They were seeded

in a 6-well plate with 1–2 mL of the culture medium until reaching 60–70% confluency, followed by incubation for 24–36 h.

Matrigel was melted overnight at 4 °C and kept on ice. Pre-sterilized 200 μL pipette tips were cooled at 4 °C, and 50 μL of Matrigel was added to each well of a pre-cooled 96-well plate, avoiding air bubbles. The plate was tapped gently and placed in a 4 °C refrigerator for 10–20 min and then transferred to a cell culture incubator for 20–30 min for solidifying.

Cell growth was monitored, and once confluency reached 80–90% with a slightly yellow medium, the supernatant was collected and centrifuged at 2000 rpm for 5 min. Healthy HUVECs were digested, counted, and resuspended to seed 12,000 to 15,000 cells/well. The collected conditioned medium was added to the resuspended cells, mixed thoroughly, and 100 μL of it was pipetted into each well of a coated 96-well plate with at least three replicate wells per concentration.

After a 10-min incubation, the cells were examined under a microscope for uniform distribution and appropriate density before returning to the incubator. The cells were observed every 2 h, with peak ring formation typically occurring at 6–8 h post-seeding. Photographs were taken to document the formation of vascular structures for counting and statistical analyses.

2.13 Subcutaneous tumor xenograft assay in nude mice

Male BALB/c nude mice, aged 5 weeks, were randomly assigned into six groups of 5 each and acclimatized for a week prior to tumor cell injection. Liver cancer cells were digested with trypsin in adherent culture, centrifuged, and resuspended in sterile PBS to create a single-cell suspension. After cell counting, the suspension was mixed with high-concentration Matrigel (1:1 ratio), and an appropriate volume of the mixture was injected into the axillary regions on both sides of the mice. Different cell densities were injected, with a volume of 100 μL per mouse. Tumor growth was monitored using the IVIS Lumina bioimaging system. After 30 days of tumor growth, the mice were anesthetized using inhaled anesthetics and euthanized via cervical dislocation. Subcutaneous tumors were excised and measured for size. Tumors were photographed against a white background and then divided into two parts: one part was fixed in 4% paraformaldehyde for subsequent pathological analysis and the other part was stored at − 80 °C for future molecular analyses. All animal experiments and experimental procedures were approved by the Ethics Committee of The First Affiliated Hospital of Anhui Medical University and also complied with the guidelines of the Guide for the Care and Use of Laboratory Animals prepared by the National Academy of Sciences and published by the National Institutes of Health (NIH Publication 86 – 23, revised 1985).

2.14 Statistical analyses

Statistical analyses were conducted using R software (v4.4.0). For pairwise comparisons between the two groups, the Wilcoxon test was employed, while the Kruskal–Wallis test was applied for comparisons among multiple groups. Survival analysis was performed using the Kaplan–Meier method and log-rank test. The optimal cutoff value for the stemness risk score was determined using the "surv_cutpoint" function from the survminer R package (v0.5.0). $p < 0.05$ was considered to indicate statistical significance.

3 Results

3.1 Landscape of stem cell gene set enrichments and identification of three stemness subtypes

The ssGSEA algorithm was used to quantify the enrichment scores of 26 stem cell gene sets for each HCC sample. Through univariate and multivariate Cox analyses, 12 prognostic stem gene sets were identified ($p < 0.05$). These gene sets were used to establish a prognostic stemness network, which highlights their interactions, lineages, and impacts on OS in patients with HCC (Fig. 1A). Based on the ssGSEA scores of the 26 gene sets, patients with HCC were stratified into three distinct clusters using unsupervised clustering through the ConsensusClusterPlus package (Fig. 1B). Spearman correlations among the ssGSEA scores of the 26 stemness-related gene sets are provided in Additional File 1: Supplementary Fig. S1A.

Among the three clusters, C1 (211 patients) and C3 (64 patients) showed significant enrichment for most stem cell gene sets, whereas C2 (226 patients) exhibited relatively low enrichment levels (Fig. 1C, D). Kaplan–Meier analysis revealed that patients with HCC in C1 had significantly poorer prognoses than those in the other clusters (log-rank $p = 0.0455$, Fig. 1E).

To further delineate the TME characteristics of the stemness subtypes, CIBERSORT and ESTIMATE analyses were conducted to evaluate TME fractions as well as immune and stromal scores (Fig. 1F). Among the three clusters, C1 exhibited immunosuppressive features, as characterized by the predominance of M0 and M2 macrophages, alongside elevated immune and stromal scores. Cluster C2 demonstrated moderate TME infiltration, with notable populations of activated memory CD4 + T cells, follicular helper T-cells, activated NK cells, M2 macrophages, and activated dendritic cells, accompanied by a prominent stromal score. Conversely, C3 was enriched with anti-tumor TME components, including CD8 + T-cells, activated memory CD4 + T-cells, M1 macrophages, and activated mast cells.

3.2 Prediction of chemotherapy sensitivity and immunotherapy response

Chemotherapy remains a cornerstone in the management of advanced HCC, while immunotherapy and targeted therapies are gaining prominence. To evaluate sensitivity to various therapeutic agents, the IC50 values for chemotherapeutic drugs, immunotherapeutics, and targeted therapies were estimated using the pRRophetic algorithm, and comparisons were made across the stem cell clusters. The IC50 values for bleomycin, bosutinib, camptothecin, cytarabine, doxorubicin, etoposide, gemcitabine, lenalidomide, methotrexate, sorafenib, and sunitinib were significantly lower in C1 (Fig. 1G), suggesting higher sensitivity of this cluster to these agents. On the other hand, clusters C2 and C3 exhibited enhanced sensitivity to elesclomol, gefitinib, imatinib, and lapatinib.

Immunotherapy responses were further analyzed using the TIDE algorithm. Reflecting the TME landscape, which highlighted enriched tumoricidal immune cell infiltration in C3, an estimated 63% of patients in C3 and 57% in C2 were predicted to benefit from immunotherapy, compared with 44% in C1 (Fig. 1H). The limited response rate in C1 may be attributed to the higher prevalence of immunosuppressive M0 and M2 macrophages, coupled with a reduced presence of M1 macrophages and CD8 + T-cells.

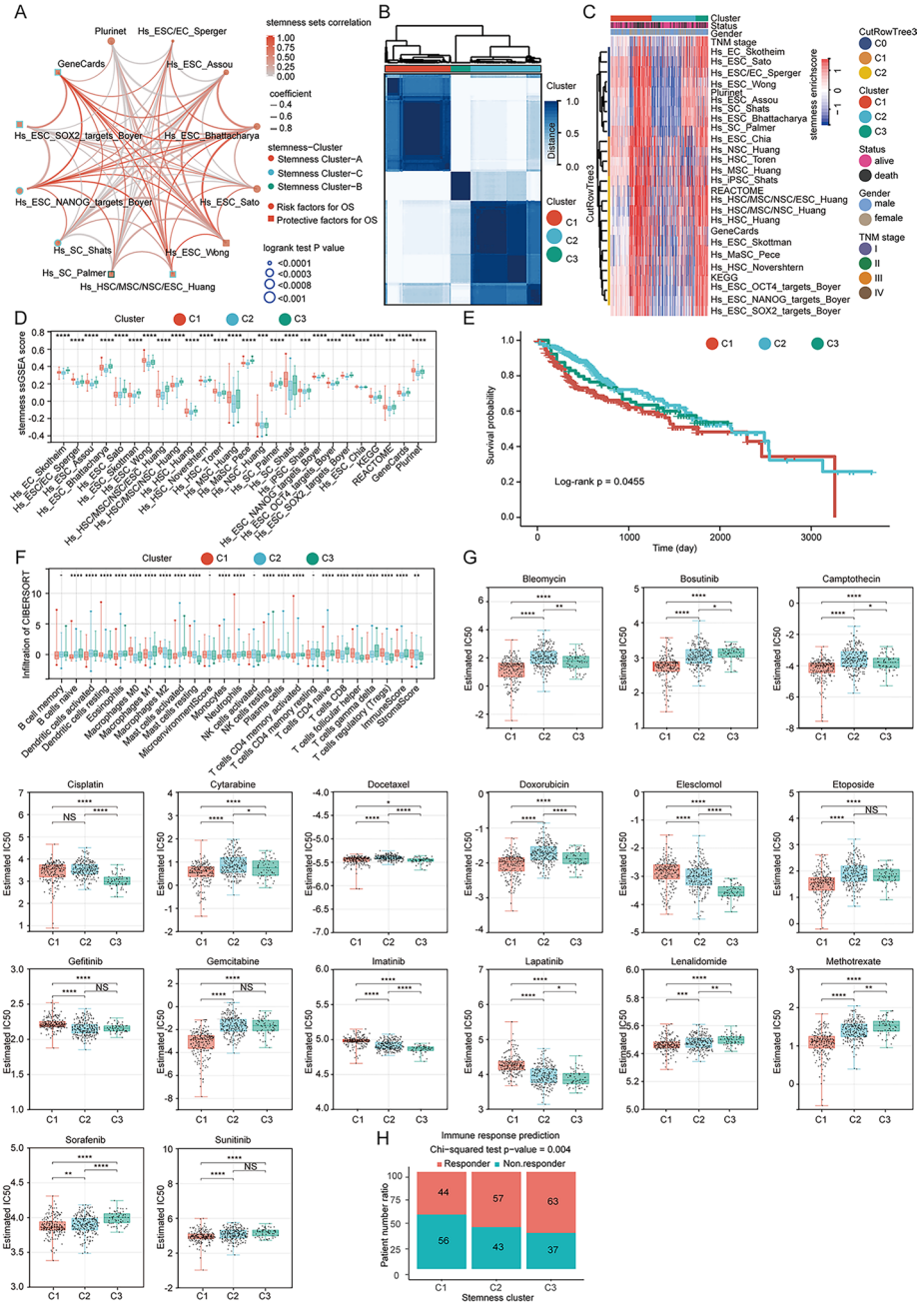

Fig. 1 Prognostic Stemness Gene Network and Clinical Implications in HCC. **A** Prognostic stemness gene network landscape in hepatocellular carcinoma (HCC) patients, illustrating the interactions, lineages, and their impacts on overall survival (OS) for 12 prognostic stemness gene sets. **B** Consensus clustering analysis revealed three distinct clusters of HCC, displaying differences in stemness gene set enrichment scores. **C** Heatmap depicting the distribution of ssGSEA stemness scores across the three clusters. **D** Box plot comparing the differences in 26 ssGSEA stemness scores among the three clusters, as assessed by the Kruskal—Wallis test, with ***$P < 0.001$. **E** Kaplan—Meier OS curves for different stemness subtypes in HCC patients. **F** Box plot illustrating the differences in 22 infiltrating immune cells, stromal, and immune scores among the three clusters, as analyzed by using the Kruskal—Wallis test; ns indicates no significance, *$P < 0.05$, **$P < 0.01$, ***$P < 0.001$. OS indicates OS and HCC denotes HCC. **G** Box plot displaying the estimated IC50 values of chemotherapy drugs among the three stemness subtypes. **H** The distribution of responders and non-responders to immunotherapy across distinct stemness clusters, as estimated by the TIDE algorithm

3.3 Construction of prognostic stemness signature and establishment and validation of a nomogram survival model

We utilized mRNA sequencing data from TCGA, comprising 342 samples, along with data from the GEO database (GSE76427 and GSE116174, containing 95 and 64 samples, respectively) to create the training dataset. The International Cancer Genome Consortium dataset, which includes 203 samples, served as an independent validation dataset. Clustering, TNM stage, and stemness risk scores were incorporated to construct a nomogram survival model.

Univariate and multivariate Cox regression analyses identified 12 stem gene sets significantly associated with HCC prognosis (Fig. 2A). Based on these gene sets, the stemness risk score was calculated, leading to the development of a nomogram for predicting prognosis (Fig. 2B). Time-dependent receiver operating characteristic analysis demonstrated that the area under the curve for OS at 1, 3, and 5 years was 0.722, 0.716, and 0.713, respectively, in the training dataset (Fig. 2C). A well-fitted calibration curve confirmed the model's predictive accuracy (Fig. 2E). Decision curve analysis indicated that the nomogram model offers a positive net benefit for patients, underscoring its clinical relevance (Fig. 2G). Using an optimal cutoff value for the stemness risk score in all 502 patients with HCC, we found that the high-stemness risk group exhibited significantly worse OS than the low-stemness risk group (log-rank test, $P = 1.9e\text{-}16$) (Fig. 2I). These findings were confirmed in the validation datasets (Fig. 2D, F, H, J). Furthermore, the distribution of patients across the three stemness clusters has been visualized in the Sankey diagram (Fig. 2K).

3.4 Identification of characteristic genes in HCC subtypes via WGCNA

Considering the poor survival outcomes and limited benefits of immunotherapy observed in patients with C1 HCC, we performed WGCNA to identify the characteristic genes in the GSE14520 cohort. To construct a scale-free network, the optimal soft-threshold power (β) was determined to be 14 (scale-free $R^2 = 0.86$) (Fig. 2L). A minimum of 30 genes per module was set, yielding 14 modules clustering genes with similar expression patterns (Fig. 2M).

Among these modules, the palevioletred 3 modules exhibited the strongest positive correlation with the C1 subtype ($ME = 0.78$, $P = 7.1e-47$) and the most significant negative correlations with the C2 subtype ($ME = -0.47$, $P = 6.9e-3$) and C3 ($ME = -0.73$, $P = 5.7e-38$). In addition, the palevioletred 3 module was moderately correlated with the survival status ($ME = -0.22$, $P = 1.1e-3$) and TNM stage ($ME = -0.32$, $P = 1.1e-6$) (Fig. 2N). Consequently, the palevioletred 3 module was selected as the hub module, yielding 23 candidate hub genes based on the filtering criteria of module membership > 0.8 and GS > 0.5 (Fig. 2O).

To explore the biological functions of the hub genes within the palevioletred 3 modules, GO and KEGG pathway enrichment analyses were conducted. The key GO terms for biological processes, cellular components, and molecular functions included small molecule metabolic processes, catabolic processes, mitochondrial function, and catalytic activity (Fig. 3A). KEGG analysis indicated that the palevioletred 3 module genes were primarily enriched in the metabolic pathways, peroxisome function, butanoate metabolism, beta-alanine metabolism, pyruvate metabolism, and tryptophan metabolism (Fig. 3B).

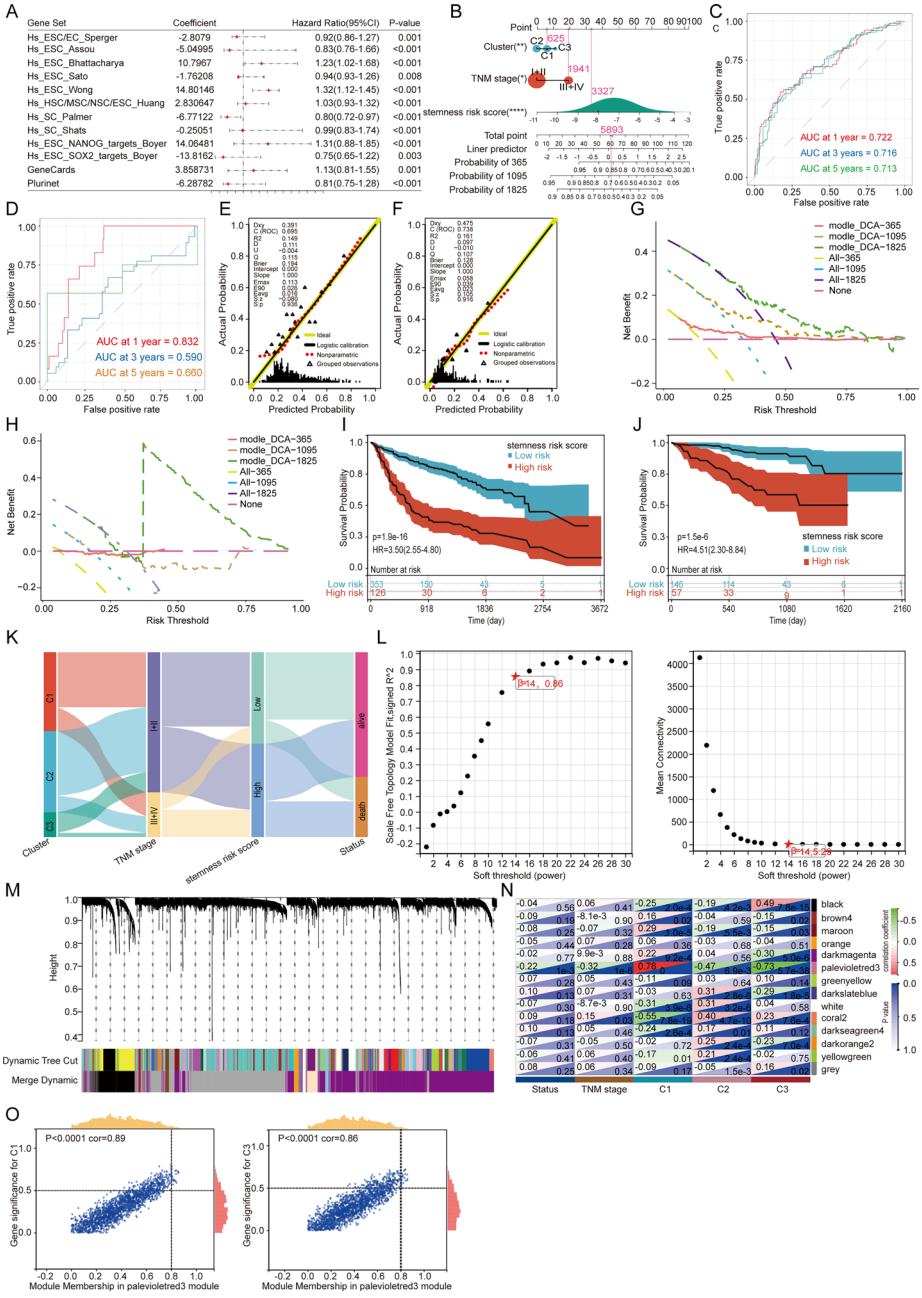

Fig. 2 Prognostic Analysis and Model Development for HCC Based on Stemness Gene Sets. **A** Forest plot illustrating the 12 prognostic stemness gene sets. **B** Analysis of the association among three distinct clusters of HCC, TNM staging, and stemness risk score with HCC prognosis led to the incorporation of prognostic factors into the development of a nomogram model. **C** Receiver operating characteristic (ROC) curves with calculated areas under the curve (AUCs) for assessing the prognostic value of the nomogram model for 1, 3, and 5 year outcomes in the training sets. **D** ROC curves for the validation sets. **E** Calibration curve diagrams for the training set indicate a good agreement between the predicted and actual probabilities, yielding S: $p > 0.05$. **F** Calibration curve diagrams for the validation set exhibiting similar results. **G** Decision curve analysis (DCA) demonstrating significant enhancement of clinical net benefit in the 1, 3, and 5 year training sets. **H** DCA results for the validation sets. **I** Kaplan—Meier survival analysis of the nomogram model in the training sets. **J** Kaplan—Meier survival analysis in the validation sets. **K** Alluvial diagram depicting the distributions of all HCC patients across different clusters, TNM staging, stemness risk score, and their survival outcomes. **L** a Scale independence and mean connectivity of multiple soft-thresholding powers (β) from 1 to 30. **M** Using the cluster dendrogram developed by weighted correlation coefficients, genes with similar expression patterns were clustered into co-expression modules, with each color representing a module. **N** Heatmap of the correlation between module eigengenes (MEs) and clinical traits as well as stemness subtypes. **O** Scatter plot displaying the relationship of module membership (MM) in the palevioletred3 module with gene significance for C1 and C3

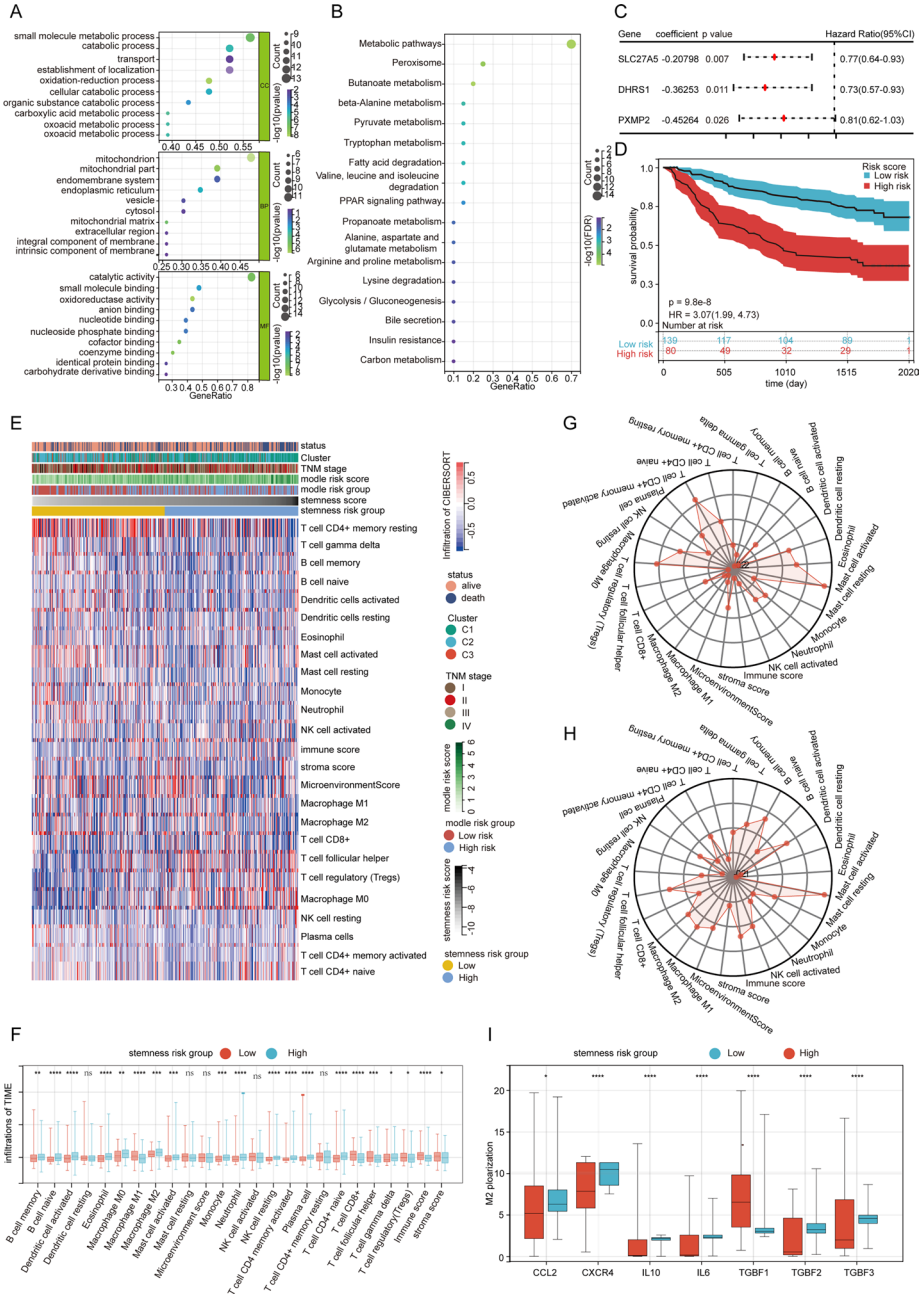

Fig. 3 Functional Enrichment and Immune Microenvironment Analysis of the Palevioletred3 Module Hub Genes. **A** The top ten enriched biological process (BP), cellular component (CC), and molecular function (MF) GO terms of palevioletred3 module hub genes. **B** KEGG analysis of Cluster palevioletred3 module hub genes. **C** Forest plot illustrating the hub genes of the palevioletred3 module, highlighting the results of univariate and multivariate Cox regression analyses associated with the prognosis of HCC patients. **D** The Kaplan—Meier survival curve of the low-risk group and the high-risk group by univariate and multivariate Cox regression analyses. **E** Heatmap manifesting the relationship between TIME infiltration and stemness-risk score as well as clinical pathological parameters. **F** The fraction of TIME cells (z-score transformed) in the high and low stemness-risk groups. Wilcoxon test, ns, not significance; *$p < 0.05$; **$p < 0.01$; ***$p < 0.001$. TIME, Tumor immune microenvironment. **G** Radar charts exhibiting the immune cell infiltration abundances in the low stemness-risk groups. **H** Radar charts showing the immune cell infiltration abundances in the high stemness-risk groups. **I** Comparison of markers associated with M2 macrophage polarization between the high and low stemness-risk groups

Univariate and multivariate Cox regression analyses further identified three hub genes significantly associated with HCC prognosis (Fig. 3C, D).

3.5 Correlation between stemness risk signature and TME infiltration patterns

Using CIBERSORT and ESTIMATE, we analyzed TME and immune cell infiltrates, including immune and stromal scores, which were visualized in a heatmap (Fig. 3E). Our findings revealed that as the stemness risk scores increased, the proportions of M0 and M2 macrophages, along with both immune and stromal scores, also increased. In contrast, the proportions of antitumor immune cells—such as M1 macrophages, activated NK cells, CD8 + T-cells, and follicular helper T-cells—were significantly lower. Wilcoxon analysis confirmed that the levels of naïve B cells, eosinophils, M0 macrophages, M2 macrophages, monocytes, neutrophils, resting NK cells, plasma cells, and naïve CD4 + T-cells were significantly higher in the high-stemness risk group than in the low-stemness risk group. Conversely, several key antitumor immune cell types, including activated dendritic cells, M1 macrophages, activated NK cells, activated memory CD4 + T-cells, CD8 + T-cells, and follicular helper T-cells, were more abundant in the low-stemness risk group than in the high-stemness risk group (Fig. 3F). In addition, the average TME distributions for each group were visualized (Fig. 3G, H). The low-stemness risk group demonstrated enhanced antitumor immunity, whereas the high-stemness risk group was dominated by immunosuppressive cells, particularly M0 and M2 macrophages. Notably, the regulators of M2 macrophage polarization were highly expressed in the high-stemness risk group (Fig. 3I).

In conclusion, these results suggested that patients in the high-stemness risk group have reduced sensitivity to immunotherapy. This finding likely reflects the immunosuppressive influence of stromal components and M2 macrophages within TME.

3.6 Stemness risk score as a predictor of chemotherapy sensitivity and immunotherapy response

Our previous results indicated that the C1 subtype was more sensitive to several chemotherapeutic agents (Fig. 1G), but exhibited reduced sensitivity to immunotherapy (Fig. 1H). Similarly, we found that the high-stemness risk group was more responsive to drugs such as bleomycin, bosutinib, camptothecin, cytarabine, cisplatin, docetaxel, elesclomol, and imatinib (Fig. 4A). We then examined the relationship between the stemness-risk model and predicted immunotherapy responses by using the TIDE method. Stemness risk scores were significantly lower in patients who responded to treatment than in nonresponders (Wilcoxon test, $p < 0.001$) (Fig. 4B). Moreover, the proportion of immunotherapy responders in the low-stemness risk group was almost double that in the high-stemness risk group (56% vs. 29%, chi-square test, $p < 0.001$) (Fig. 4C). The model was further applied to a real-world immunotherapy cohort (the IMvigor210 cohort, treated with anti-PD-L1). In this cohort, responders to anti-PD-L1 therapy had significantly lower stemness risk scores than nonresponders (Wilcoxon test, $p = 8.0e\text{-}3$) (Fig. 4D). Additionally, patients in the high-stemness risk group showed significantly lesser benefit from treatment than those in the low-stemness risk group (20% vs. 30%, chi-square test, $p = 0.036$) (Fig. 4E). Survival analysis also revealed that patients in the high-stemness risk group had significantly shorter survival times than those in the

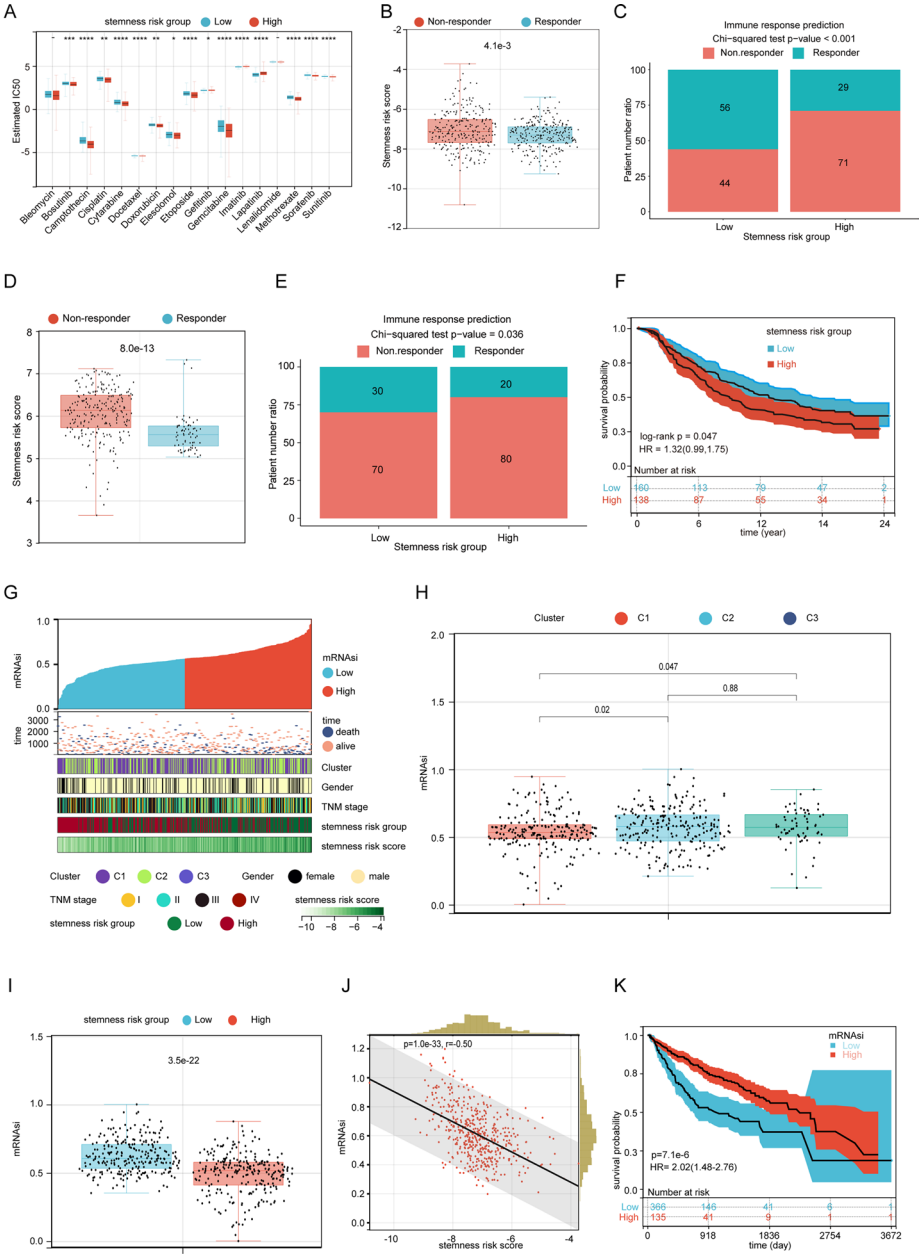

Fig. 4 Chemotherapy Response and Stemness Risk Analysis in HCC. **A** Box plots of the estimated IC50 values of several chemotherapy drugs between the high and low-stemness-risk groups. **B** TIDE results of the differences in the stemness-risk score between the respond and non-respond groups. **C** The distributions of responder and non-responder across distinct stemness-risk groups. **D** Differences in the stemness-risk score in SD/PD and CR/PR groups in the IMvigor210 cohort. **E** The distributions of anti-PD-L1 therapeutic response in distinct stemness-risk groups in the IMvigor210 cohort. **F** Kaplan–Meier survival analysis revealed a high stemness-risk score, which was correlated with a worse prognosis in the IMvigor210 cohort. **G** The overview of the correlation between mRNAsi and clinical features as well as stemness clusters and risk scores. **H** Box plot showing the comparison of the mRNAsi among three stemness Clusters. **I** Box plot of the comparison of the mRNAsi among the stemness-risk groups. **J** The Spearman correlation of stemness-risk score with mRNAsi. **K** Kaplan–Meier survival analysis revealed high mRNAsi, which was correlated with a better prognosis in HCC patients

low-stemness risk group (hazard ratio = 1.32, 95% confidence interval: 0.99–1.75, log-rank $p = 0.047$) (Fig. 4F).

3.7 mRNAsi levels were reduced in C1 and negatively correlated with the stemness risk score

Using the OCLR algorithm, we calculated the mRNAsi for each HCC patient based on the gene expression profiles and subsequently examined the relationship between mRNAsi and stemness subtypes. Ranking mRNAsi from low (left panel) to high (right panel), we observed that the C1 stemness subtype was primarily located in regions with low mRNAsi (Fig. 4G), whereas the C2 and C3 subtypes exhibited the highest mRNAsi, as confirmed by comparative analysis (Fig. 4H). Moreover, the low-stemness risk group had significantly higher mRNAsi (Wilcoxon test, $p = 3.5e\text{-}22$) (Fig. 4I), and a strong negative correlation was found between mRNAsi and the stemness risk score (Spearman correlation = – 0.50, $p = 1.0e\text{-}33$) (Fig. 4J). Kaplan–Meier analysis also indicated that patients with HCC with low mRNAsi had poorer OS than those with high mRNAsi (Fig. 4K).

3.8 Low expression of PXMP2 correlates with improved survival in HCC

Among the three genes examined, *PXMP2* was identified as the most significant gene associated with HCC stemness through ssGSEA stemness scoring, with higher expression correlating with better patient prognosis(Supplementary Fig. S1B and S1C). We have now incorporated a systematic pan-cancer analysis of PXMP2 expression using TCGA data (new Supplementary Fig. S1D), revealing that PXMP2 exhibits significantly higher expression in HCC compared to other cancer types. To further validate its potential role, we functionally assessed *PXMP2* in relation to LCSC properties (Fig. 5A, B). Analysis of the TCGA database revealed that the *PXMP2* expression was closely associated with tumorigenesis and CSC pathways, including the PI3K-Akt, Wnt, and Hippo signaling pathways (Fig. 5C).

The study of tumor and adjacent tissues from 36 patients, as well as tissue microarrays from 90 patients revealed that *PXMP2* transcription was significantly reduced in the tumor tissues than in the paired adjacent tissues (Fig. 5D–F). Furthermore, tissue microarray analysis confirmed that low *PXMP2* expression was associated with poorer prognosis in patients with HCC (Fig. 5G). The low *PXMP2* expression also correlated with advanced tumor stage and increased metastasis (Supplementary Fig. S2A and S2B).

Multiplex fluorescence immunohistochemistry revealed a negative correlation between *PXMP2* expression and the stemness markers ANPEP and SOX2 in HCC tissues (Fig. 5H,I, J). Both ANPEP and SOX2 were associated with poor prognosis in HCC (Supplementary Fig. S2C and S2D). Single-cell bioinformatics analysis of liver cancer revealed that *PXMP2* expression was lower in liver LCSCs than in hepatocytes (Fig. 5K–N). Moreover, *PXMP2* levels were higher in M1 macrophages than in M2 macrophages, while the expression in neutrophils was relatively low (Fig. 5L and Supplementary Fig. S3D).

3.9 *PXMP2* knockdown promotes the proliferation and recruit or regulate M2 macrophage infiltration of HCC cells

We successfully inhibited *PXMP2* expression in 3B cells using specific shRNAs (shPXMP2-1, shPXMP2-2, and shPXMP2-3) (Supplementary Fig. S3A and 6 C). To

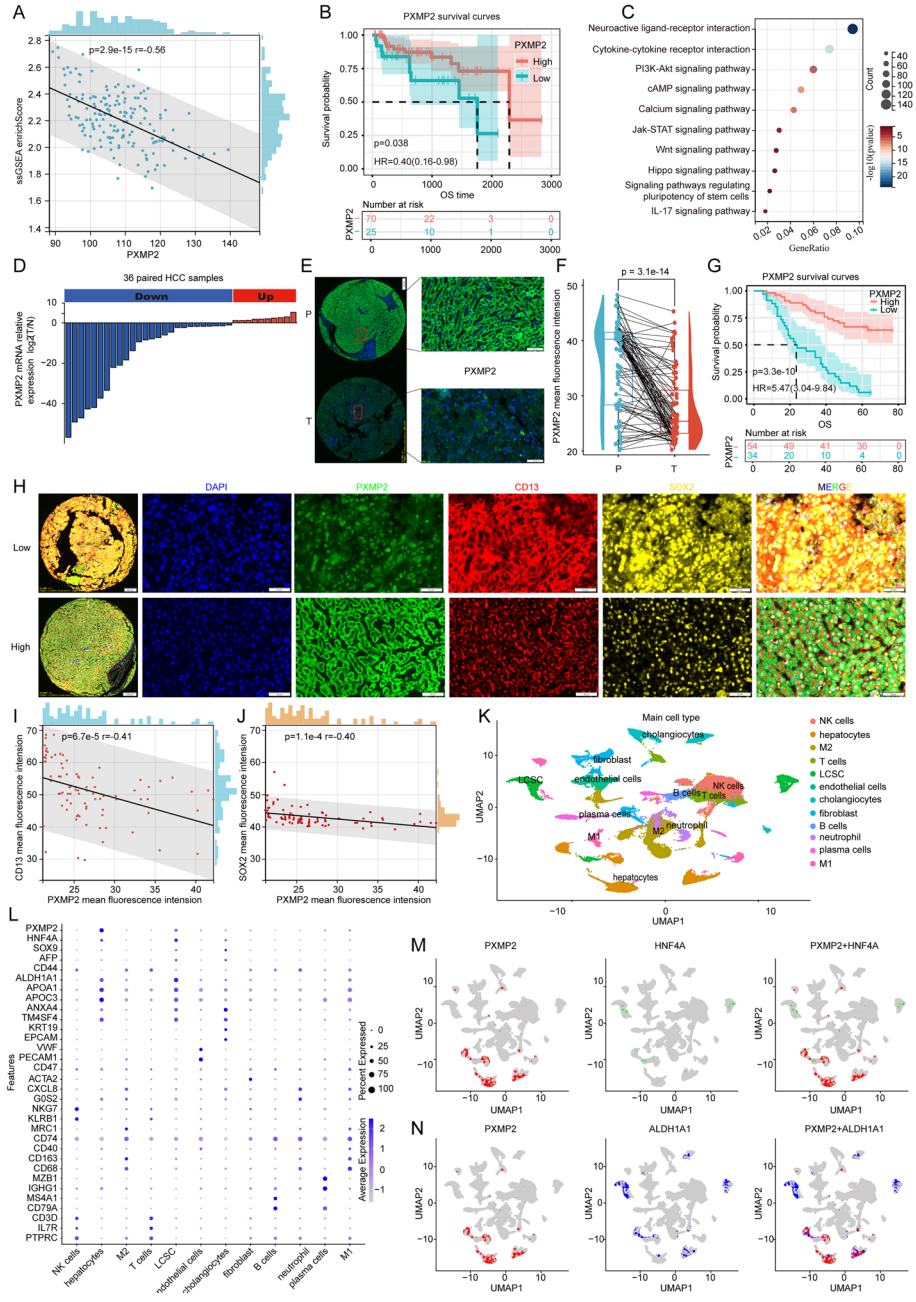

Fig. 5 Clinical Analysis of PXMP2 in HCC. **A** The Spearman correlation between PXMP2 and the ssGSEA stemness enrichment score. **B** Kaplan–Meier survival analysis revealed the correlation of high PXMP2 with a better prognosis in HCC patients using TCGA. **C** Top KEGG pathways associated with differentially expressed genes between the high and low expression groups of PXMP2. **D** A bidirectional bar chart illustrating the expression of PXMP2 in 36 pairs of HCC tumors and adjacent non-tumor tissues. **E** Immunofluorescence staining of the PXMP2 expression in HCC tumors and adjacent non-tumor tissues through tissue microarrays. **F** A paired raincloud plot depicting the mean fluorescence intensity of the PXMP2 expression in HCC tumors and adjacent non-tumor tissues using tissue microarrays. **G** Kaplan–Meier survival analysis revealed that a high PXMP2 expression was correlated with a better prognosis in HCC patients through tissue microarrays. **H** Representative images of PXMP2 (green), CD13 (red), and SOX2 (yellow) in HCC patients using tissue microarrays. Nuclei were stained with DAPI (blue). Scale bar = 50 μm. **I** A scatter plot illustrating the correlation between the mean fluorescence intensity of PXMP2 and CD13 by tissue microarrays. **J** A scatter plot illustrating the correlation between the mean fluorescence intensity of PXMP2 and SOX2 using tissue microarrays. **K** Joint UMAP visualization of cell types and subclusters. **L** The expression of markers for the 12 clusters, as well as the expression of PXMP2 and stemness indicators, was assessed. **M** PXMP2 co-expresses with LCSC marker HNF4A in distinct clusters. **N** PXMP2 Co-expresses with stemness marker ALDH1A1 in distinct clusters

assess the stemness characteristics of *PXMP2*, limiting dilution analysis was performed. The results revealed that transfection with shPXMP2-1 and shPXMP2-2 significantly increased both the number and size of spheres in 3B cells (Supplementary Fig. S3B and Fig. 6D), indicating enhanced stemness properties in HCC cells (Fig. 6A, B).

In the transwell assay, silencing *PXMP2* in 3B cells significantly enhanced their migration and invasion abilities (Fig. 6E). The colony formation assay further revealed that *PXMP2* silencing promoted the proliferation of HCC cells (Fig. 6F). In addition, the tube formation assay showed that tumor angiogenesis capacity was significantly increased when *PXMP2* was silenced (Fig. 6G).

To evaluate the in vivo effects of shPXMP2, tumorigenesis was assessed using limiting dilution assays (Supplementary Fig. S3C). Hep3B cells with shPXMP2 showed significantly increased tumorigenesis (Fig. 6H–J). Multiplex fluorescence immunohistochemistry revealed that *PXMP2* knockdown enhanced the expression of stemness markers ANPEP and SOX2 within tumor tissues (Fig. 6K).

To further explore the potential connection between *PXMP2* and the tumor immune microenvironment, we examined immune cell infiltration in tumor tissues. Our findings demonstrated that *PXMP2* knockdown promoted the infiltration of M2 macrophages and neutrophils while suppressing M1 macrophage infiltration (Fig. 6L). These findings provide additional evidence of the close association between *PXMP2* and tumor stemness, suggesting that reduced *PXMP2* expression facilitates the infiltration of M2 macrophages and neutrophils, which contributes to tumor progression.

3.10 PXMP2 inhibits HCC progression through the PI3K/AKT/mTOR and WNT pathways

In both in vivo and in vitro studies, *PXMP2* knockdown significantly enhanced the proliferation and metastasis of HCC cells. To identify the biological functions and signaling pathways associated with *PXMP2*, we performed KEGG and GO enrichment analyses by categorizing *PXMP2* expression into high and low groups (Fig. 5C). The analysis revealed that the PI3K-AKT and WNT-signaling pathways were primarily linked to *PXMP2* expression in HCC (Fig. 7A, B). To further validate these findings, we conducted Western blotting to assess protein alterations in the PI3K-AKT and WNT pathways following *PXMP2* silencing in 3B cells.

Our results showed that silencing *PXMP2* did not affect the AKT protein levels, rather led to increased levels of phosphorylated AKT, β-catenin, and phosphorylated β-catenin (Fig. 7C). These changes were further confirmed through multiplex fluorescence immunohistochemistry, which revealed similar alterations in these pathway proteins in vivo (Fig. 7D, E). These results suggested that *PXMP2* knockdown promoted HCC progression by activating the PI3K-AKT and WNT-signaling pathways.

These findings establish PXMP2 as a critical oncogenic driver in HCC that exerts its tumor-promoting effects through dual activation of PI3K-AKT and WNT/β-catenin signaling pathways (Supplementary Fig. S3E, F). Using specific pharmacological inhibitors (MK-2206 and MSAB), we demonstrate that PXMP2 knockdown enhances multiple malignant phenotypes including tumor stemness (Fig. 7F), proliferation (Fig. 7G), 3D growth (Fig. 7H), and angiogenesis(Fig. 7I), all of which are completely reversed by pathway inhibition. Our results not only elucidate the mechanistic basis of PXMP2-mediated HCC progression but also identify PI3K-AKT and WNT signaling as promising therapeutic targets for HCC patients with elevated PXMP2 expression, highlighting the

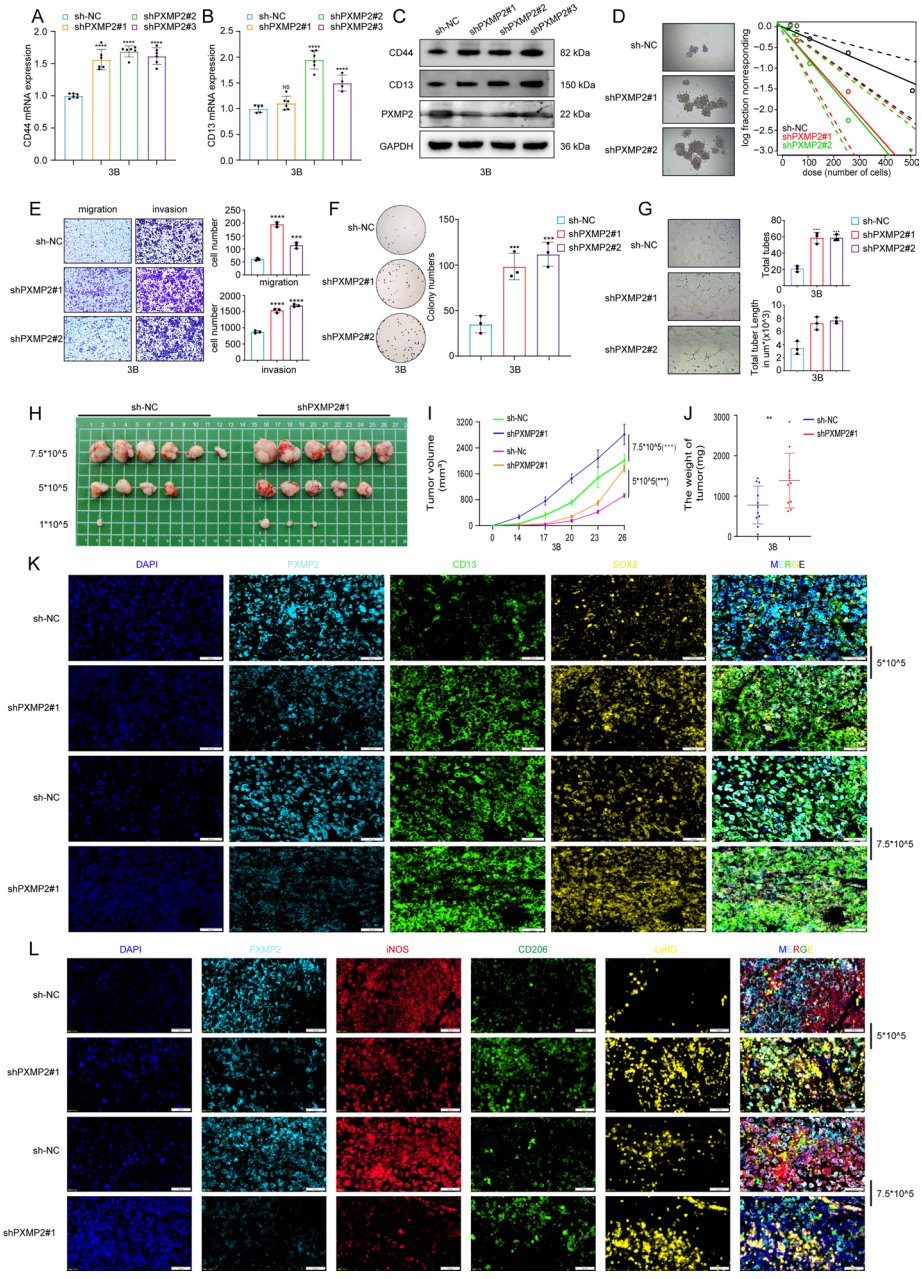

Fig. 6 Functional Analysis of PXMP2 Knockdown in HCC Cells. **A** qRT-PCR displaying the induction of CD44 mRNA expression in 3B cells by shPXMP2 treatment. **B** qRT-PCR showing the induction of the CD13 mRNA expression in 3B cells by shPXMP2 treatment. **C** Western blotting shows the expression of PXMP2, CD44, and CD13 protein in 3B cells via shPXMP2 treatment. **D** 3B frequency with shPXMP2 treatments was determined by using in vitro limiting dilution analysis (LDA). **E** Transwell detection of changes in the migration of 3B after treatment with shPXMP2. **F** Colony formation abilities of 3B with shPXMP2 treatments. **G** The effect of 3B cells with shPXMP2 treatments on the function of HUVES cells was detected by angiogenesis assay. **H** The gross examination demonstrated a drastic reduction in the tumor size in all dilutions of sh-NC cells as compared to that in the shPXMP2 group of the same cell concentration. **I** In vivo growth of shPXMP2-treated 3B cells was significantly accelerated. **J** The tumor volume of 3B cells processed with shPXMP2 was significantly larger. **K** In the tumor tissue of 3B cells treated with shPXMP2, the expression of PXMP2 was significantly decreased, while the expression of stemness markers CD13 and SOX2 were increased. **L** In the tumor tissues of 3B cells treated with shPXMP2, the expression of the M1 macrophage marker iNOS was decreased, while the expressions of the M2 macrophage marker CD206 and the neutrophil marker Ly6G were increased

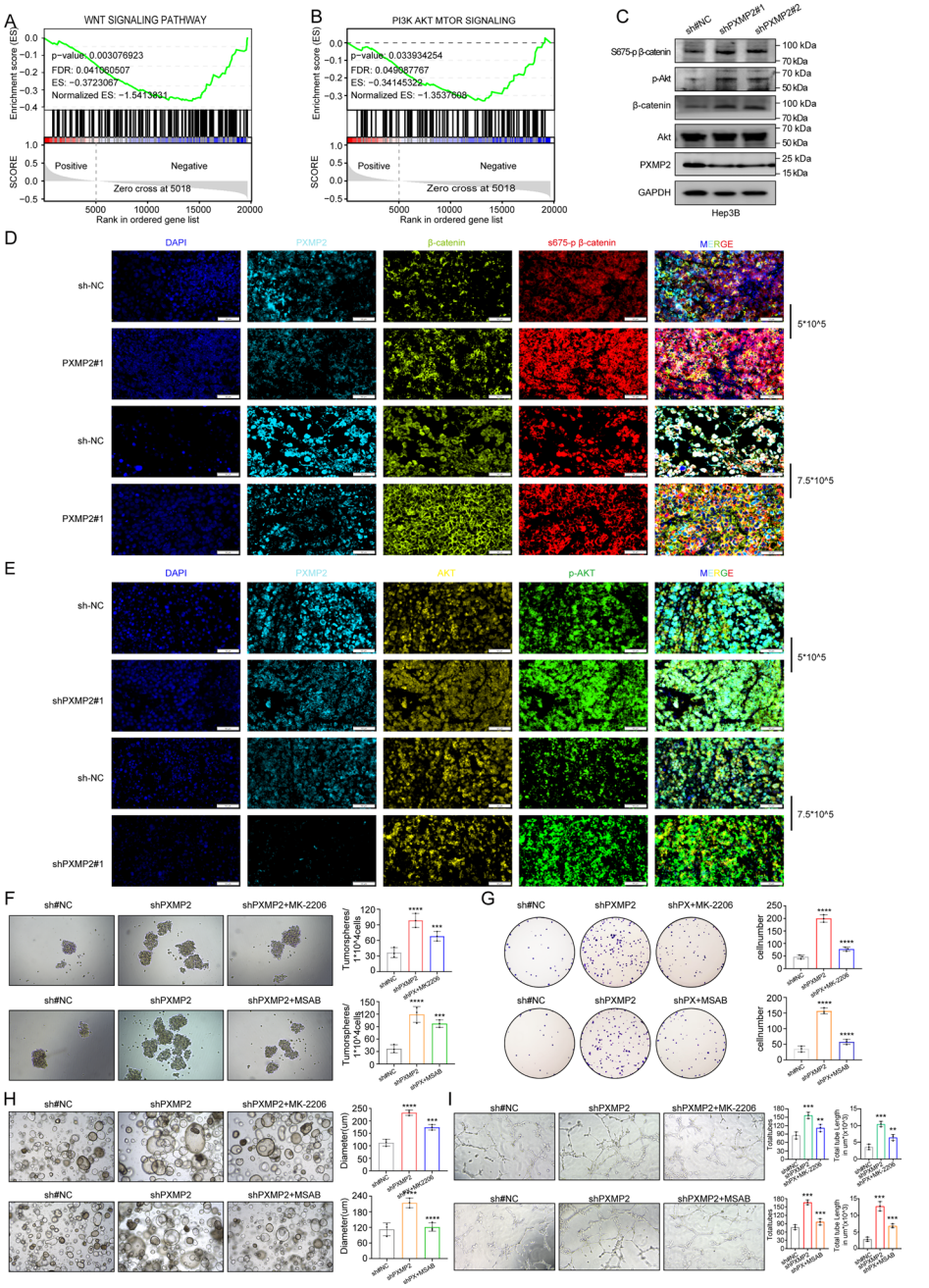

Fig. 7 Pathway Analysis Following PXMP2 Knockdown in HCC Cells. **A** GSEA analysis displaying the enrichment of WNT signaling pathway genes in the low PXMP2 group and significant downregulation of the same in the high PXMP2 group using TCGA. **B** GSEA analysis shows the enrichment of PI3K AKT MTOR signaling genes in the low PXMP2 group and the significant downregulation of the same in the high PXMP2 group using TCGA. **C** 3B cells treated with shPXMP2, the expression of p-AKT, β-catenin, and p-β-catenin was significantly increased by Western blotting. **D** The tumor volume of 3B cells treated with shPXMP2, the expression of β-catenin and p-β-catenin was significantly increased. **E** In the tumor volume of 3B cells treated with shPXMP2, the expression of p-AKT was significantly increased. **F** Effects of shPXMP2 on 3B frequency and rescue assay with pathway inhibitors. **G** 3B frequency analysis by colony formation assay with shPXMP2 and pathway inhibitor rescue. **H** Effects of shPXMP2 on 3B frequency in patient-derived liver cancer organoids and rescue with pathway inhibitors. **I** Effects of shPXMP2 on 3B frequency in vascular formation assay and rescue with pathway inhibitors

potential clinical utility of pathway-specific inhibitors in this molecularly defined HCC subtype.

4 Discussion

HCC, which is one of the most prevalent and aggressive malignancies, is characterized by a high incidence and poor patient prognosis [17]. A defining feature of HCC is the presence of CSCs, a distinct subpopulation of tumor cells that play a pivotal role in tumor initiation, progression, and resistance to therapy [18]. In liver CSCs, several highly conserved signaling pathways, including Wnt/β-catenin, Notch, and Hedgehog, are aberrantly activated, which contributes to their stemness and malignancy. Moreover, key transcription factors such as NANOG, OCT4, SOX2, and cMYC are essential for maintaining the self-renewal and proliferative capabilities of these CSCs [19]. Recent advances in research have increasingly focused on deciphering the regulatory mechanisms governing liver CSCs, thereby providing deeper insights into their biology and highlighting potential therapeutic targets to improve the treatment outcomes. Despite improvements in the survival rates with surgical intervention and adjuvant postoperative therapy, treatment outcomes in HCC remain suboptimal due to challenges such as drug resistance and variability in patient sensitivity and tolerance to treatment. As such, exploring more personalized therapeutic approaches, which are tailored to the specific characteristics of the tumor and predicted treatment outcomes, may offer opportunities to improve efficacy and extend survival.

With increasing recognition of the critical role that immune activity plays in tumor initiation, progression, and prognosis, immunotherapy has emerged as a promising approach to cancer treatment [20]. A growing array of immunotherapeutic agents, such as pembrolizumab, ipilimumab, and nivolumab, have been approved and shown to yield beneficial effects in various cancer types [21]. This surge in immunotherapy has highlighted the urgent need for identifying sensitive and reliable immune-related biomarkers, including immune response genes.

LCSCs are known to remodel TME into an immunosuppressive landscape through both extrinsic and intrinsic mechanisms, ultimately leading to immune evasion [22]. However, a comprehensive understanding of how LCSCs influence prognosis in HCC and their interaction with the TME and immunotherapy remains lacking. This gap in knowledge underscores the importance of further research to better utilize LCSCs in therapeutic strategies.

In this study, we performed a detailed bioinformatics analysis to explore the molecular features of 26 CSC gene sets across a large multicenter cohort of patients with HCC. We hypothesize that precise molecular subtyping based on stemness characteristics can enhance the stratification of patients with HCC, thereby enabling more accurate predictions of prognosis, TME infiltration patterns, and responses to treatment. Understanding the gene expression patterns associated with CSC subtypes could provide new avenues for developing personalized therapies that target specific aspects of tumor biology.

Through unsupervised clustering of ssGSEA scores derived from the 26 stemness gene sets, we identified three distinct stemness clusters. C1 exhibited a distinct immunosuppressive phenotype, as characterized by an abundance of M0 and M2 macrophages, as well as elevated immune and stromal scores. C2 showed moderate TME infiltration, with

a notable presence of activated memory CD4 + T-cells, follicular helper T-cells, activated NK cells, M2 macrophages, and activated dendritic cells, alongside prominent stromal scoring. In contrast, C3 was enriched in antitumor immune components, including CD8 + T-cells, activated memory CD4 + T-cells, M1 macrophages, and activated mast cells.

To further investigate the prognostic potential of these subtypes, we constructed a nomogram model based on the prognostic signatures derived from these stemness clusters. After model training and validation, we demonstrated that this nomogram could offer significant clinical benefits for patients with HCC. In addition, to delve deeper into the genomic underpinnings of the stemness subtypes, we conducted WGCNA to identify co-expressed gene modules linked to the clusters. The palevioletred 3 module, which was strongly positively correlated with C1 and negatively correlated with C2 and C3, emerged as the most relevant module for further investigation. We then performed univariate Cox and random forest survival analyses to identify prognostic hub genes within this module, which led to the development of a stemness prognostic signature composed of three key genes (*SLC27A5*, *DHRS1*, and *PXMP2*), which effectively quantified the stemness patterns. Consistently, stemness risk scores were highest in C1, and elevated scores correlated with poorer prognosis in patients with HCC.

TME has become increasingly recognized for its influence on cancer prognosis. Past studies have consistently demonstrated the impact of TME on patient outcomes [23], and research by Soysal has underscored its importance in breast cancer [24]. In addition, the role of tumor immunity in prognosis and clinical decision-making has gained significant attention. Galon's study highlighted the value of immune architecture and immune scoring in predicting cancer outcomes, particularly in cholangiocarcinoma patients [25], thereby further supporting the idea that comprehending the TME is crucial to understanding cancer prognosis and treatment.

In our analysis, we observed that patients with HCC with lower stemness risk exhibited robust antitumor immunity, as evidenced by the higher infiltration of CD4 + memory-activated T-cells, CD8 + T-cells, and M1 macrophages. In contrast, the high-stemness risk group displayed a greater presence of immunosuppressive cells, particularly M0 and M2 macrophages, along with stromal components. Notably, the abundance of M2 macrophages and M0 macrophages in the high-stemness risk group suggested that M2 polarization plays a significant role in driving immunosuppression and promoting tumor invasiveness. These findings align with those of previous studies indicating that M2 macrophages contribute to immune evasion in cancer [26, 27]. Furthermore, we observed that the TIDE score, a predictive marker for immune evasion, was significantly higher in the high-stemness risk group than in the low-stemness risk group. This finding suggests that patients with low stemness risk scores are more likely to benefit from immune checkpoint inhibitors, while those with high-risk scores may have reduced sensitivity to immunotherapy. This model was also validated by using the IMvigor210 cohort [28], thereby reinforcing the potential of our stemness risk score as a tool for predicting patient response to immunotherapy.

Malta et al. developed the transcriptomic stemness index (mRNAsi) using the OCLR method, which quantifies the activity of CSCs and the malignant dedifferentiation of tumor samples [29]. Notably, our stemness risk model shows a significant negative

correlation with the mRNA stemness index (correlation coefficient = – 0.50), suggesting that our model effectively reflects the stemness characteristics in HCC.

Among the three genes identified in our stemness model, *PXMP2* has not yet been extensively studied in the context of tumor stemness. However, its homologous protein, PXMP4, promotes epithelial–mesenchymal transition in gastric cancer cells via the PI3K/AKT-signaling pathway. PXMP2, a member of the peroxisomal membrane protein family, is involved in key metabolic processes. Moreover, the disruption of peroxisomal function leads to significant metabolic changes in liver cancer cells, which ultimately inhibit their proliferation. However, the precise mechanisms through which PXMP2 influences liver cancer cells remain unclear. Our findings suggest that PXMP2 impacts the stemness phenotype of liver cancer cells through modulation of the WNT signaling pathway. The biogenesis of peroxisomes involves membrane formation and the targeting of membrane proteins [30], which are processes that are critical for cellular metabolism. Peroxisomal redox metabolism plays a role in modulating immune responses, including the activation of nuclear factor kappa-light-chain-enhancer of activated B cells. Furthermore, peroxisomal β-oxidation and ether lipid synthesis are crucial in the development and activation of both innate and adaptive immune cells. As the number and metabolic activity of peroxisomes are associated with inflammatory diseases, PXMP2 may play a significant role in antitumor immunity.

Despite the valuable insights provided by this study, there are several limitations to consider. First, our analysis relies on publicly available datasets, which introduces the possibility of bias and limits the generalizability of our findings. Second, the prognostic and therapeutic efficacy of the stemness risk model has not been validated in a large, independent cohort from our center. Moreover, while bioinformatics analyses have identified model genes, further functional studies are warranted to explore their biological roles in stemness, TME interactions, and their potential as therapeutic targets. Notably, the cancer-type specificity of PXMP2's function warrants systematic investigation in future studies. While our current findings demonstrate the crucial role of PXMP2 in modulating stemness properties through WNT/β-catenin signaling in HCC, its potential tissue-specific functions across different malignancies (e.g., gastric or colorectal cancers) remain to be elucidated. Comprehensive cross-cancer analyses incorporating single-cell RNA sequencing and spatial transcriptomics approaches will be essential to delineate the context-dependent regulatory networks of PXMP2 in diverse tumor microenvironments.

5 Conclusion

In conclusion, we identified three distinct stemness-related subtypes of HCC with differential prognoses, TME profiles, and treatment responses using unsupervised clustering of the stem cell gene set. A nomogram model based on this gene set was developed and externally validated through Cox and random survival forest analyses. Furthermore, we established a three-gene risk model linked to stemness, which was validated in a large cohort of patients with HCC using WGCNA, Cox, and random survival forest approaches. Our findings highlight the clinical utility of this stemness model in prognostic assessment and its potential to guide clinicians in identifying patients who are most likely to benefit from immune checkpoint inhibitor therapies.

Supplementary Information

The online version contains supplementary material available at https://doi.org/10.1007/s12672-025-02976-4.

Supplementary Material 1

Acknowledgements
Not applicable.

Author contributions
D.Y., Q.W., Q.X. and B.S. designed the overall experiments, analyzed data, and wrote the manuscript. D.Y., J.C. and J.W. performed most of the experiments. Q.G., X. H. and J.Q. performed animal experiments. T.F., S.M. and R.W. performed immunofluorescence staining in HCC specimens. Q.X. and B.S. designed the overall experiments, analyzed data, D.Y. and Q.W. wrote the main manuscript. J.C prepared Figs. 1, 2 and 3. Q.G. and J.W. prepared Figs. 4 and 5. X. H. and J.Q. prepared figures 6. T.F. and S.M. prepared figures 6. R.W. prepared figures s1-3. All authors reviewed the manuscript.

Funding
This research was supported by grants from the State Key Program of the National Natural Science Foundation (82120108012 and 81930086 to B.S.; 82372755 to Q.W.), Clinical Research Special Project of Anhui Provincial Department of Science and Technology (Grand number: 202204295107020008 to B.S.) and Research Program of Anhui Provincial Department of Education (Grand number: 2022AH010070 to B.S.). This work was partly supported by Natural Science Foundation of Anhui Province (2408085Y040 to Q.W.), Research Fund of Anhui Institute of translational medicine (2022zhyx-C21 to Q.W.), and Outstanding Youth Scientific Research Projects in colleges and universities of Anhui Province (2022AH030115 to Q.W.).

Data availability
The datasets used and/or analyzed during the current study are available from the corresponding author on reasonable request.

Declarations

Ethics approval and consent to participate
In the study, all experimental procedures were approved by the Ethics Committee of The First Affiliated Hospital of Anhui Medical University and conformed to the requirements of the Declaration of Helsinki and the International Ethical Guidelines for Biomedical Research Involving Human Subjects. Clinical samples were obtained with informed consent from 90 HCC patients who underwent surgery between 2016 and 2018 at the First Affiliated Hospital of Anhui Medical University (AHMU). All animal experiments and experimental procedures were approved by the Ethics Committee of The First Affiliated Hospital of Anhui Medical University and also complied with the guidelines of the Guide for the Care and Use of Laboratory Animals prepared by the National Academy of Sciences and published by the National Institutes of Health (NIH Publication 86 – 23, revised 1985), which permits the inclusion of mouses with tumor sizes up to 2.0 cm in maximal diameter. The maximal tumor burden was maintained below 5% of the animal's total body weight in all experimental subjects, with therapeutic studies permitting an upper threshold of 10% as per institutional guidelines.

Consent for publication
Not applicable.

Competing interests
The authors declare no competing interests.

Received: 25 March 2025 / Accepted: 11 June 2025
Published online: 18 June 2025

References

1. Ferlay J, Soerjomataram I, Dikshit R, et al. Cancer incidence and mortality worldwide: sources, methods and major patterns in GLOBOCAN 2012. Int J Cancer. 2015;136(5):E359–86. https://doi.org/10.1002/ijc.29210.
2. Llovet JM, Montal R, Villanueva A. Randomized trials and endpoints in advanced HCC: role of PFS as a surrogate of survival. J Hepatol. 2019;70(6):1262–77. https://doi.org/10.1016/j.jhep.2019.01.028.
3. Heimbach JK, Kulik LM, Finn RS, et al. AASLD guidelines for the treatment of hepatocellular carcinoma. Hepatology. 2018;67(1):358–80. https://doi.org/10.1002/hep.29086.
4. Kuhlmann JB, Blum HE. Locoregional therapy for cholangiocarcinoma. Curr Opin Gastroenterol. 2013;29(3):324–8. https://doi.org/10.1097/MOG.0b013e32835d9dea.
5. Brown ZJ, Tsilimigras DI, Ruff SM, et al. Management of hepatocellular carcinoma: A review. JAMA Surg. 2023;158(4):410–20. https://doi.org/10.1001/jamasurg.2022.7989.
6. Liu YC, Yeh CT, Lin KH. Cancer stem cell functions in hepatocellular carcinoma and comprehensive therapeutic strategies. Cells. 2020;9(6):1331. https://doi.org/10.3390/cells9061331.
7. Kim CF, Jackson EL, Woolfenden AE, et al. Identification of bronchioalveolar stem cells in normal lung and lung cancer. Cell. 2005;121(6):823–35. https://doi.org/10.1016/j.cell.2005.03.032.
8. Hermann PC, Huber SL, Herrler T, et al. Distinct populations of cancer stem cells determine tumor growth and metastatic activity in human pancreatic cancer. Cell Stem Cell. 2007;1(3):313–23. https://doi.org/10.1016/j.stem.2007.06.002.
9. Li C, Heidt DG, Dalerba P, et al. Identification of pancreatic cancer stem cells. Cancer Res. 2007;67(3):1030–7. https://doi.org/10.1158/0008-5472.CAN-06-2030.

10. O'Brien CA, Pollett A, Gallinger S, et al. A human colon cancer cell capable of initiating tumour growth in immunodeficient mice. Nature. 2007;445(7123):106–10. https://doi.org/10.1038/nature05372.
11. Maugeri-Sacca M, Vigneri P, De Maria R. Cancer stem cells and chemosensitivity. Clin Cancer Res. 2011;17:4942–7. https://doi.org/10.1158/1078-0432.CCR-10-2538.
12. Ji J, Wang XW. Clinical implications of cancer stem cell biology in hepatocellular carcinoma. Semin Oncol. 2012;39(4):461–72. https://doi.org/10.1053/j.seminoncol.2012.05.011.
13. Batlle E, Clevers H. Cancer stem cells revisited. Nat Med. 2017;23(10):1124–34. https://doi.org/10.1038/nm.4409.
14. Fan ST, Yang ZF, Ho DW, et al. Prediction of posthepatectomy recurrence of hepatocellular carcinoma by Circulating cancer stem cells: a prospective study. Ann Surg. 2011;254(4):569–76. https://doi.org/10.1097/SLA.0b013e3182300a1d.
15. Philip PA, Mooney M, Jaffe D, et al. Consensus report of the National cancer Institute clinical trials planning meeting on pancreas cancer treatment. J Clin Oncol. 2009;27(33):5660–9. https://doi.org/10.1200/JCO.2009.21.9022.
16. Taminau J, Meganck S, Lazar C, et al. Unlocking the potential of publicly available microarray data using InSilicoDb and insilicomerging r/bioconductor packages. BMC Bioinformatics. 2012;13:335. https://doi.org/10.1186/1471-2105-13-335.
17. Vidal SJ, Rodriguez-Bravo V, Galsky M, et al. Targeting cancer stem cells to suppress acquired chemotherapy resistance. Oncogene. 2014;33(36):4451–63. https://doi.org/10.1038/onc.2013.411.
18. Wang Q, Liang N, Yang T, et al. DNMT1-mediated methylation of BEX1 regulates stemness and tumorigenicity in liver cancer. J Hepatol. 2021;75(5):1142–53. https://doi.org/10.1016/j.jhep.2021.06.025.
19. Kather JN, Halama N, Jaeger D. Genomics and emerging biomarkers for immunotherapy of colorectal cancer. Semin Cancer Biol. 2018;52(Pt 2):189–97. https://doi.org/10.1016/j.semcancer.2018.02.010.
20. Tintelnot J, Stein A. Immunotherapy in colorectal cancer: available clinical evidence, challenges and novel approaches. World J Gastroenterol. 2019;25(29):3920–8. https://doi.org/10.3748/wjg.v25.i29.3920.
21. Dai X, Guo Y, Hu Y, et al. Immunotherapy for targeting cancer stem cells in hepatocellular carcinoma. Theranostics. 2021;11(7):3489–501. https://doi.org/10.7150/thno.54648.
22. Petitprez F, Vano YA, Becht E, et al. Transcriptomic analysis of the tumor microenvironment to guide prognosis and immunotherapies. Cancer Immunol Immunother. 2018;67(6):981–8. https://doi.org/10.1007/s00262-017-2058-z.
23. Soysal SD, Tzankov A, Muenst SE. Role of the tumor microenvironment in breast Cancer. Pathobiology. 2015;82(3–4):142–52. https://doi.org/10.1159/000430499.
24. Bruni D, Angell HK, Galon J. The immune contexture and immunoscore in cancer prognosis and therapeutic efficacy. Nat Rev Cancer. 2020;20(11):662–80. https://doi.org/10.1038/s41568-020-0285-7.
25. Najafi M, Hashemi Goradel N, Farhood B, et al. Macrophage Polarity in cancer: A review. J Cell Biochem. 2019;120(3):2756–65. https://doi.org/10.1002/jcb.27646.
26. Osman A, Oze M, Afify SM, et al. Tumor-associated macrophages derived from cancer stem cells. Acta Histochem. 2020;122(8):151628. https://doi.org/10.1016/j.acthis.2020.151628.
27. Jiang P, Gu S, Pan D, et al. Signatures of T cell dysfunction and exclusion predict cancer immunotherapy response. Nat Med. 2018;24(10):1550–8. https://doi.org/10.1038/s41591-018-0136-1.
28. Malta TM, Sokolov A, Gentles AJ, et al. Machine learning identifies stemness features associated with oncogenic dedifferentiation. Cell. 2018;173(2):338–e35415. https://doi.org/10.1016/j.cell.2018.03.034.
29. Costello JL, Schrader M. Unloosing the gordian knot of peroxisome formation. Curr Opin Cell Biol. 2018;50:50–6. https://doi.org/10.1016/j.ceb.2018.02.002.
30. Di Cara F, Savary S, Kovacs WJ, et al. The peroxisome: an up-and-coming organelle in immunometabolism. Trends Cell Biol. 2023;33(1):70–86. https://doi.org/10.1016/j.tcb.2022.06.001.

Publisher's note